

# Investigation of Microstructural Features Determining the Toughness of 980 MPa Bainitic Weld Metal

R. CAO, X.B. ZHANG, Z. WANG, Y. PENG, W.S. DU, Z.L. TIAN, and J.H. CHEN

The microstructural features that control the impact toughness of weld metals of a 980 MPa 8 pct Ni high-strength steel are investigated using instrumented Charpy V tester, optical microscope (OM), scanning electron microscope (SEM), transmission electron microscope (TEM), electron back-scattered diffraction (EBSD), and finite-element method (FEM) calculation. The results show that the critical event for cleavage fracture in this high-strength steel and weld metals is the propagation of a bainite packet-sized crack across the packet boundary into contiguous packets, and the bainitic packet sizes control the impact toughness. The high-angle misorientation boundaries detected in a bainite packet by EBSD form fine tear ridges on fracture surfaces. However, they are not the decisive factors controlling the cleavage fracture. The effects of Ni content are essential factors for improving the toughness. The extra large cleavage facets seriously deteriorate the toughness, which are formed on the interfaces of large columnar crystals growing in welding pools with high heat input.

DOI: 10.1007/s11661-013-2020-4

© The Minerals, Metals & Materials Society and ASM International 2013

## I. INTRODUCTION

WITH sustained improvement of the properties of high-strength steels, the impact toughness has reached around 200J at lower temperatures of 223 K ( $-50\text{ }^{\circ}\text{C}$ ) for 980 MPa grade steels.<sup>[1]</sup> However, the toughness of the weld metal with matching strength is appreciably lower than this value. How to increase the toughness of weld metal through the modification of the microstructure has been attracting a the attention of welding metallurgists.

Before the 1980s, the microstructural feature that controlled the impact toughness was identified as the ferrite grain size.<sup>[2]</sup> Reference 3 illustrated that both ends of fracture facets coincided with the packet boundaries in the lath structure or the grain boundaries in blocky transformation products. The effective grain size, which controls the toughness, was determined by the packet width in lath structure and ferrite grain size in the blocky transformation products. In tempered martensite, the effective grain size was dependent on the austenite grain size, which explained the austenite size dependency of the toughness of tempered martensite steels.

From the 1980s, the critical event controlling brittle fracture at low temperatures has been generally considered

as the propagation of a particle crack, and the presence of brittle particle alone would be determinant for the brittle fracture process.<sup>[4]</sup> Reference 5 indicated that in the transition region, the critical fracture stress  $\sigma_f$  defined the cleavage fracture in reactor pressure vessel (RPV) steels, and its value obtained from the mean diameter of the carbides only above some critical size, quantitatively 1 pct of the total population, were in good agreement with the values from the finite-element method (FEM) calculations.

However, Reference 6 pointed out that in their study it appears that grain size, as well as the surrounding microstructure, had a significant influence. The susceptibility to cleavage fracture did not depend on the size of the fracture initiating particle but additionally on the local ferrite grain size. The higher sensitivity to cleavage fracture of coarse-grained microstructures demonstrated the modulating influence of the grain size in microstructures with a substantial presence of cleavage inducing brittle particles.

In bainitic steels, Reference 7 revealed that when the austenite grain size was large, each grain was transformed into several bainitic grains. As the austenite grain size decreased, the number of bainitic packets per austenite grain dropped until a ratio of 1:1 was reached. The bainitic packet size measured by electron back-scattered diffraction (EBSD) with a 15 deg misorientation criterion was about 3.5 times less than the value determined by optical microscopy, and it was identified as the microstructural unit controlling crack propagation in a cleavage fracture. In this case, the unit crack path (UCP) size oscillated between 7.7  $\mu\text{m}$  and 8.8  $\mu\text{m}$ , and the effective surface energy of cleavage fracture  $\gamma_p$  varied between 71.6  $\text{J m}^{-2}$  and 82.6  $\text{J m}^{-2}$ .

In martensite steels, Reference 8 found that the impact toughness is controlled by the martensite packet size in quenched as well as in moderately tempered low-carbon lath martensite.

---

R. CAO and J.H. CHEN, Professors, and Z. WANG, Master, are with the State Key Laboratory of Gansu Advanced Non-ferrous Metallic Materials and Key Laboratory of Non-ferrous Metal Alloys of the Ministry of Education, Lanzhou University of Technology, Lanzhou 730050, P.R. China. Contact e-mail: zchen@lut.cn X.B. ZHANG, Doctor, is with the Department of Materials Science and Engineering, Shanghai Jiaotong University, Shanghai 200240, P.R. China. Y. PENG, W.S. DU, and Z.L. TIAN, Professors, are with the Central Iron and Steel Research Institute, Beijing 100081, P.R. China.

Manuscript submitted February 5, 2013.

Article published online October 16, 2013

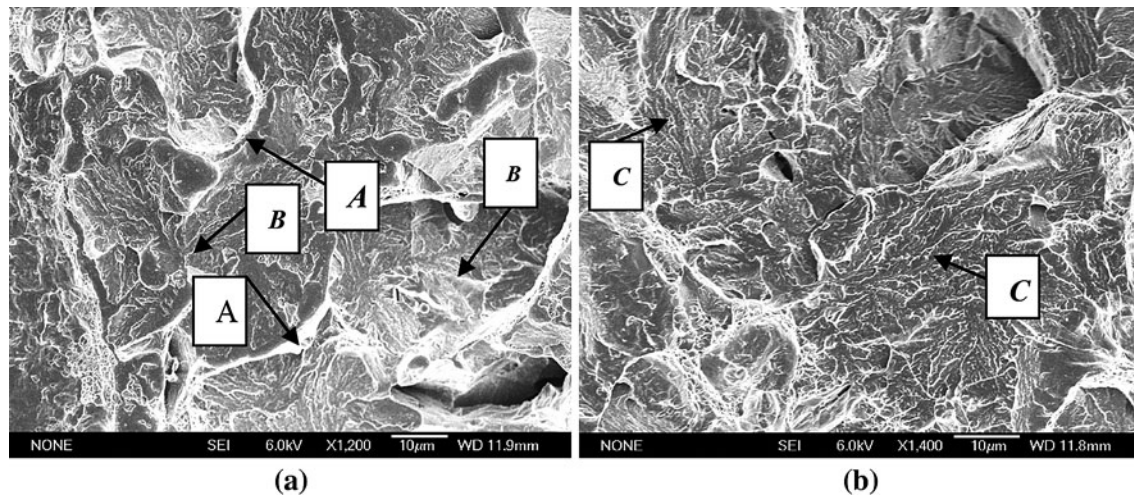


Fig. 1—Three barriers against propagation of cleavage cracking: the original austenite grain boundaries, pointed by allow *A* in (a); the tear ridges made of the bainite colony (packet) boundaries, pointed by allow *B* in (a) and the parallel fine tear ridges made of the inter layers between bainitic laths, pointed by allow *C* in (b).

In addition, on the effects of nickel addition, regardless of packet size and yield strength, the addition of nickel gave rise to a decrease in Charpy V impact transition temperature of about 293 K (20 °C) per pct nickel.<sup>[8]</sup> Nickel additions also moderated the sensitivity to grain size and yield strength of the impact transition temperature.<sup>[8]</sup> These strong intrinsic toughness improvement effects of nickel addition should mainly be attributed to increases in cleavage fracture resistance and only to a minor extent to a solute-softening effect on the yield strength. In our previous work, the current authors found three barriers resisting against the propagation of cleavage cracking.<sup>[9]</sup> The typical quasi-cleavage facet in Figure 1 shows three types of barriers resistant to crack extension: the wide dimple belts made of the original austenite grain boundaries (pointed by allow *A* in Figure 1(a)), the tear ridges made of the bainite colony (packet) boundaries (pointed by allow *B* in Figure 1(a)), and the parallel fine tear ridges made of the inter layers between bainitic laths (pointed by allow *C* in Figure 1(b)).

From the above review, the microstructural parameter, which controls the toughness of weld metal, may be the grain size, martensite or bainite packet size, the size of area with misorientation angle larger than 15 deg, and the brittle second phase particle size. In this work, we use instrumented Charpy V tester, optical microscope (OM), scanning electron microscope (SEM), transmission electron microscope (TEM), EBSD, and FEM calculations to identify which one in the above microstructural parameters really controls the fracture and the toughness of impact Charpy V specimens. In addition, the effects of nickel addition are analyzed.

## II. EXPERIMENTAL

### A. Materials

Base metal (BM) is a 980 MPa 8 pct Ni high-strength steel that is used for the maritime vessel at the lowest temperature of 223 K (−50 °C). Six weld metals with

various nickel contents were applied for welding this base metal. The compositions of these metals are listed in Table I. T5-21 is a Tungsten inert gas arc welding (TIG) weld metal containing around 6 pct nickel. DM4-1 is an metal active gas arc welding (MAG) weld metal containing around 3.5 pct nickel. M100 and T100 are two weld metals containing about 6 pct nickel and are welded by MAG and TIG with horizontal weaving. The weld regimes are listed in Table II.

### B. Tensile Tests

Standard tensile tests were carried out by Shimadzu AG-10T universal test machine (Shimadzu Corporation, Kyoto, Japan) with cross-head speed of 1mm/min at various temperatures. The round specimens of dimensions shown in Figure 2(a) were used.

### C. Charpy V Tests

Charpy V impact tests were conducted at various temperatures by instrumented impact machine CIEM-300-CPC (Hitachi Limited, Tokyo, Japan) with standard specimen shown in Figure 2(b). For estimating the composite toughness of a multipass weld and the solidification path of the weld with high levels of nickel, the notch tip was cut in the middle of the multipass weldment as shown in Figure 2(c). The macrostructure in the way of cracking is shown in Figure 2(d), which including the reheated center part (noted by Figure 2(c)) and the upper and lower parts of as-deposited multipass welds (noted by Figures 2(a) and (b)).

### D. Observation of Metallograph for Characterizing the Microstructural Features and Measuring Grain and Packet Sizes Under the Fracture Surface

Metallographs are prepared by grinding and polishing the fracture surface of the Charpy specimen fractured at 223 K (−50 °C) to characterize the microstructural

**Table I. Compositions of Experimental Metals (wt pct)**

Sample	C	S	P	Cr	Ni	Si + Mn + Mo + Cu + Nb + V
BM	0.08	0.002	0.008	0.60	7.58	1.77
T5-21	0.07	0.005	0.005	0.71	5.74	2.71
DM4-1	0.07	0.005	0.008	0.70	3.79	2.46
M100	0.09	0.010	0.006	0.65	6.18	2.82
T100	0.07	0.004	0.008	0.63	6.36	2.7

**Table II. Welding Method and Working Condition**

Welding Method	No.	Heat Input (KJ/mm)	Shielding Gas	Arc Current (A)
TIG	T5-21	2.0	Ar	300
MAG	DM4-1	1.6	Ar + 5 pct CO <sub>2</sub>	280
MAG	M100	1.6	Ar + 5 pct CO <sub>2</sub>	280
TIG	T100	2.0	Ar	300

M100 and T100 welding with horizontal weaving.

features just under the fracture surface as shown in Figure 3(a). For measuring the austenite grain sizes, the specimens were etched by the picric acid, and for measuring the packet column sizes, the specimens were etched by nital.

#### E. Electron Back-scattered Diffraction (EBSD) for Measuring the High Angle Boundary

A ZEISS ULTRA 55 field-emission scanning electron microscope (Carl Zeiss, Oberkochen, Germany) was used to collect EBSD grain boundary maps and to define the orientations of microstructural features. To get high-resolution maps of the microstructure, the step size was set to 0.1  $\mu\text{m}$ . All the maps were analyzed using the Oxford Instruments Channel 5 HKL suite of programs (Oxford Instruments, Oxfordshire, U.K.).

#### F. Observation of Fracture Surfaces and Measurement of the Fracture Initiation Distance

The general features and the details of fracture facets were observed on the fracture surfaces. The distances  $X_f$  from the blunted crack tip to the site of cleavage cracking initiation were measured on the fracture surfaces of specimens that were fractured at lower temperatures without or with short fibrous crack extension. The distances  $X_f$  is a very important parameter by which the local fracture stress  $\sigma_f$  is calculated. The nature of crack-initiating particles was characterized.

#### G. Observation of the Retained Cracks to Identify the Critical Event for Cleavage Fracture that Was Related to the Microstructural Features

The critical event, which controls cleavage fracture, is defined as the stage offering the most difficulty during the crack initiation and propagation. The critical event

can be revealed by the cracks that retained in the fractured specimen. Metallographic sections were prepared by cutting the specimens perpendicularly to the notch roots for observation of retained cracks close to the fracture surfaces as shown in Figure 3(b). The event of the crack propagating across the boundary of the microstructural feature that contains the retained crack is identified as the critical event. The lengths of retained cracks were measured by Image software.

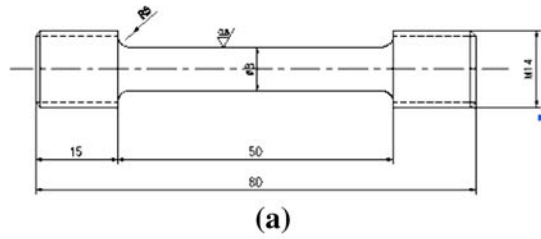
#### H. Finite-Element Method (FEM) for Calculating the Microcritical Fracture Parameter $\sigma_f$

A three-dimensional model with eight-node biquadratic plane-strain-reduced integration elements (C3D8R) of ABAQUS code was used to calculate the normal stress ( $\sigma_{yy}$ ) distribution in the Charpy V specimen with a notch root of 0.25 mm (shown in Figures 4(a) and (b)). The C3D6 elements were used for the transition region. Thirty elements were arranged around the notch root (shown in Figure 4(c)). The total element numbers were 6912 and node numbers were 9480. The dynamic load mode in Abaqus code was used for the calculation of the Charpy V specimen. By inserting the measured fracture distance  $X_f$  as the abscissa into the distribution curves of  $\sigma_{yy}$  for fractured specimens, the corresponding ordinates were taken as the local fracture stress  $\sigma_f$ . Because the data measured by instrumented Charpy V machine in dynamic condition fluctuated violently, the calculation results were not as accurate as calculated in the static condition.

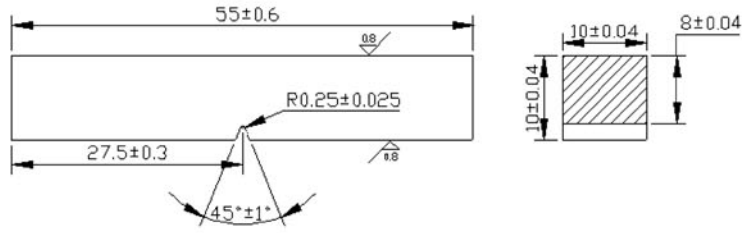
### III. EXPERIMENTAL RESULTS

#### A. Results of Tensile and Charpy V Tests

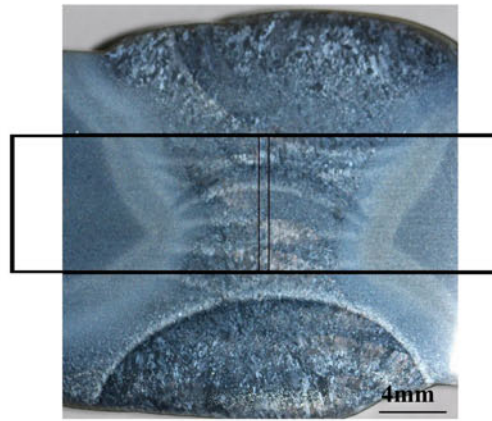
The data measured by tensile tests at 223 K ( $-50^\circ\text{C}$ ) and measured by impact tests at 77 K ( $-196^\circ\text{C}$ ) are listed in Table III. The values of impact toughness



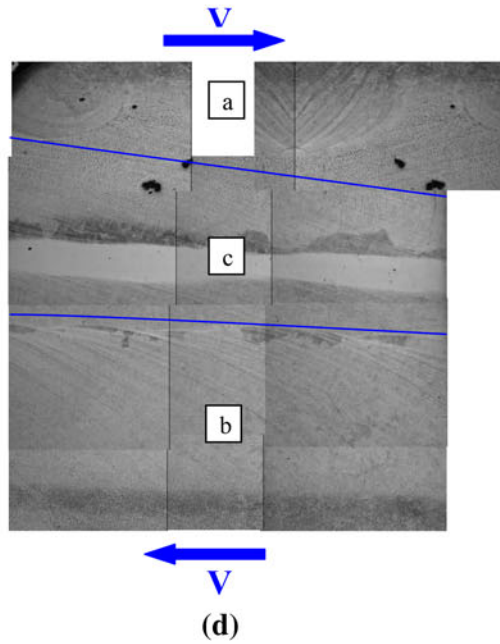
(a)



(b)



(c)



(d)

Fig. 2—Dimensions of (a) tensile specimen and (b) Charpy V Specimen. (c) Location of the notch of Charpy V specimen. (d) Microstructure in the way of cracking.



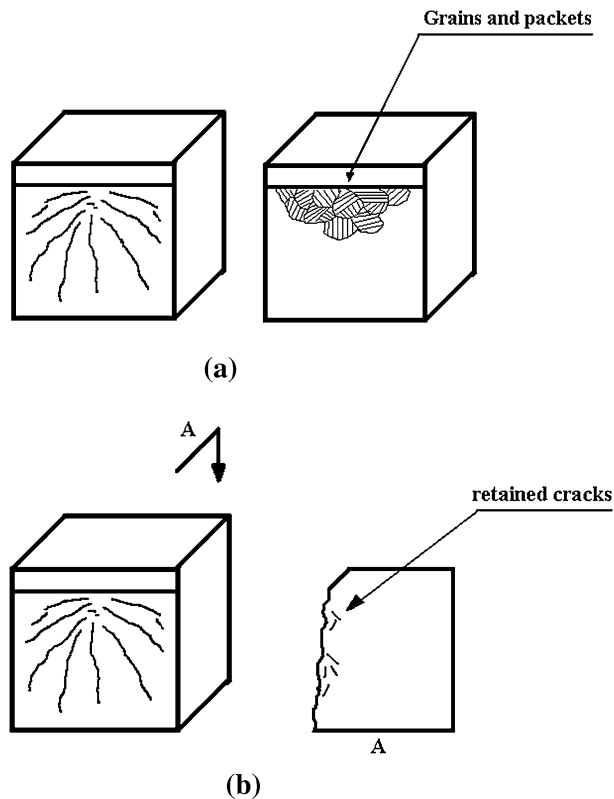


Fig. 3—Schematic (a) preparing the metallograph for observation of the microstructural features just under the fracture surface. (b) Preparing the metallographic section for observation of retained cracks.

measured by the instrumented Charpy V tester at a temperature range from 77 K to 293 K ( $-196\text{ }^{\circ}\text{C}$  to  $20\text{ }^{\circ}\text{C}$ ) are plotted in Figure 5. Table IV lists the impact toughness values measured at 223 K and 77 K ( $-50\text{ }^{\circ}\text{C}$  and  $-96\text{ }^{\circ}\text{C}$ ).

From Table IV and Figure 5, it is found that the base metal and weld metals can be divided to two groups according to the toughness measured at 223 K ( $-50\text{ }^{\circ}\text{C}$ ). The first group includes the base metal and T5-21 weld metals that present a much higher impact toughness of around 160J at 223 K ( $-50\text{ }^{\circ}\text{C}$ ). The second group includes DM4-1, M100, and T100, which show an appreciable lower impact toughness (lower than 60J). In the following, comparisons of the microstructural features between these two groups are carried out in the order of: (1) grain size, (2) packet size, (3) area contained by the high degree misorientation boundary, (4) width of bainitic lath, and (5) the microstructural features making the critical event for cleavage fracture. The comparisons of the above microstructural features are focused to find the decisive factors that determine the difference of the cryogenic low-temperature impact toughness between these two groups in the high-strength steel and weld metals.

## B. Results of Microstructure Observation

### 1. Microstructure

Figure 6 displays the general microstructures of base metal and all weld metals. As seen in Figure 6, the

microstructures of the first group of base metal and T5-21 weld metal are the tempered lath bainite. The microstructure of the second group of DM4-1 show the appearance of globular bainite with some acicular ferrite. The distinct characteristics of weld metals of M100 and T100 are the larger columnar grains with black trips, which are considered to be traces of segregation on the boundaries of columnar crystals growing in the weld pools. Although some differences in microstructures were observed between these two groups, the remarked difference in the impact toughness of metals cannot be simply attributed to the difference of microstructures between these two groups.

### 2. Measurement of grain size under the fracture surface close the site of crack initiation

Figure 7 displays the measurements of grain sizes of the base and weld metals on the metallograph under the fracture surface close the site of crack initiation. Figure 8 shows the histograms of the grain sizes for the base metal and weld metals. As seen in Figure 7 and Figure 8, the grain sizes of the first group of the base metal and T5-21 are appreciably finer than that of the second group of DM4-1, M100, and T100. In the weld metals of M100 and T100, the segregation traces of impurities on the boundaries of crystalline cells appear in the metallography in Figures 7(e) and (f).

### 3. Measurements of bainitic packets

Figure 9 displays the histograms of the packet sizes measured in the base metal and weld metals. As seen in Figure 9, the packet sizes of the second group of DM4-1, M100, and T100 (shown in Figures 9(c) through (e)) are larger than those of the first group of T5-21 and base metal (shown in Figures 9(a) and (b)). Figure 10 summarizes the measured results of grain and packet sizes, which also show the packet sizes of the first group are less than that of the second group.

## C. Higher Degree Misorientation Boundaries Depicted by EBSD

Figure 11 presents the higher degree misorientation boundaries depicted by EBSD for base metal and weld metals.

Figure 12 exhibits the histograms of the degrees of grain or packet boundaries. As shown in Figure 12, there are no obvious differences of the densities of high-degree misorientation boundaries revealed by EBSD between the first group of T5-21 weld metal and the second group of DM4-1 weld metal. To be surprised, the density of high-degree misorientation boundaries in the base metal is appreciably lower than those of weld metals.

## D. Observation by TEM

Figure 13 displays the TEM images of base and weld metals. Table V lists the metallographic parameters

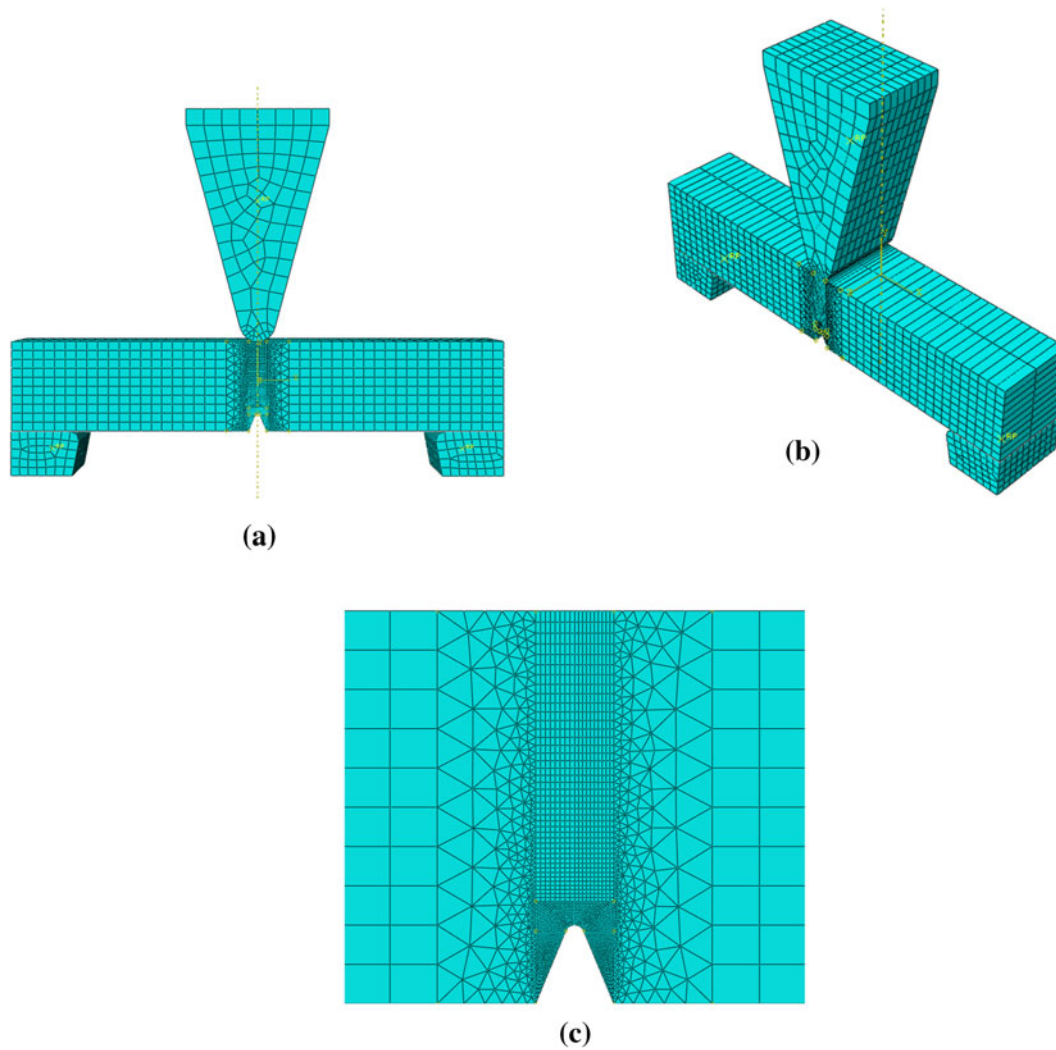


Fig. 4—Three-dimensional FEM mesh arrangement for calculation of notched Charpy V specimen.

**Table III. The Measured Results by Tensile Tests at 223 K (−50 °C) and the Impact Yield Strength at 77 K (−196 °C)**

No.	$\sigma_y$ (MPa)	$\sigma_b$ (MPa)	$\delta$ (pct)	$\Psi$ (pct)	$\sigma_{yd}$ [77K (−196 °C)] (MPa)
Base metal	1106.71	1187.12	20.39	68.59	1237
T5-21	940.33	1096.47	19.82	67.32	—
DM4-1	978.85	1115.76	11.14	56.69	1237
M100	960.39	1174.28	16.40	66.75	1158
T100	935.73	1146.98	16.45	66.30	1123

Note:  $\sigma_y$ : yield strength;  $\sigma_b$ : tensile strength;  $\delta$ : percentage elongation after fracture;  $\psi$ : percentage reduction of area;  $\sigma_{yd}$  [77K (−196 °C)]: impact yield strength measured at 77 K (−196 °C).

measured by TEM. As seen in Figure 13 and Table V, the TEM images of the base metal and all weld metals exhibit the lath structures. The base metal and the T5-21 weld metal show the finest laths, whereas the DM4-1 weld metal shows the coarsest. Black retaining austenite flakes (austenite-rich M-A constituent identified by selected-area electron diffraction [SAED]) appear at the lath boundaries in Reference 1.

#### E. Observation of Retained Cracks Relevant to the Grain or Packet Sizes

Figure 14 shows the cracks retained in base metal and weld metals in Charpy V specimens fractured at 77 K (−196 °C). The lengths of retained cracks and the lengths of packets measured by random events are plotted in right side figures.

From Figure 14, it is revealed that the retained cracks are contained in bainitic packets and the lengths of retained cracks have a consistent relationship with the lengths of randomly measured packets. In the second group of DM4-1, M100, and T100, the retained cracks corresponding to longer packet sizes were appreciably longer than that of the first group of the base metal.

#### F. Results of Fracture Surface Observation

Figure 15 displays the fractography of Charpy V specimens of the base metal and weld metal fractured at 223 K (−50 °C). The fracture surfaces of the base metal and T5-21 exhibit ductile rupture mode with dimple appearance. The DM4-1 was fractured in cleavage mode and initiated at an inclusion particle in Figure 15(d). It is worth it to indicate that on the fracture surfaces of M100, and especially of T100, brittle strips as long as 2000 μm were observed, which were apparently to be produced at boundaries of columnar crystals growing in welding pools.

### IV. DISCUSSION

#### A. Critical Event

As stated in the introduction, the critical event is the most difficult step in the crack nucleation and propagation process, which controls the cleavage fracture. The main methodology for identifying the critical event was

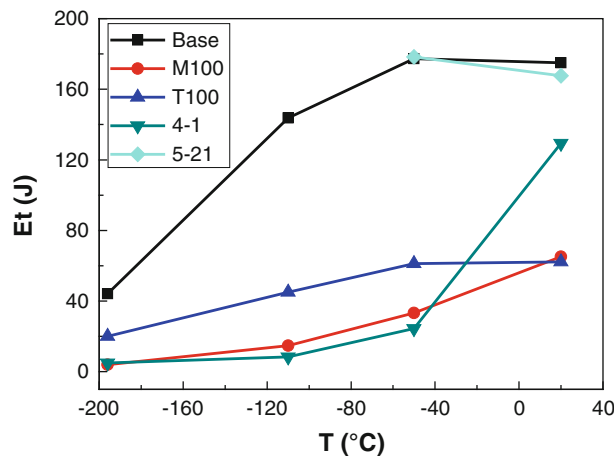


Fig. 5—Charpy V values measured at various temperatures for various specimens.

suggested by the current author<sup>[10]</sup> and described in Section II–G. Figure 14 shows the results of observations. From Figure 14 in the metallographic sections of the fractured specimens, the cracks stopped at the packet boundaries; thus, retained cracks were constrained in the bainitic packets in the base metal, DM4-1, M100, and T100. And as seen in Figures 14(b), (d), (f), and (h), there is a consistent relationship between the lengths of the retained cracks and the sizes of the bainitic packets. Based on these experimental observations, the critical events that control cleavage fracture in base metal and the weld metals are identified as the propagation of a packet-sized crack across the packet boundary into contiguous packets.

#### B. Critical Microparameters

Using the FEM described in Section II–H, the distributions of the local stress for base metal and weld metals were obtained. The values of  $\sigma_f$  were obtained as the values of the corresponding ordinates by inserting the fracture distance  $X_f$  as the abscissa. The values of  $\sigma_f$  for the first group of the base metal and the second group of the weld metal DM4-1, T100, and M100 are listed in Table IV. The corresponding impact toughness measured at 77 K (−196 °C) and at 223 K (−50 °C) are also listed in the Table IV. As seen in the Table IV, the local fracture stress  $\sigma_f$  measured in the base metal is much higher than those measured in the weld metal DM4-1, T100, and M100, and the values of  $\sigma_f$  are consistent with the values of impact toughness.

Table IV also lists the effective surface energy  $\gamma_p$  calculated from the  $\sigma_f$  and the area of the cleavage facet observed in front of the crack initiation site by equation

$$\sigma_f = \sqrt{\pi E \gamma_p / (1 - \nu^2) a} \quad (\text{for a penny-shaped crack})$$

The sizes of the cleavage facets observed in front of the crack initiation sites listed in Table IV are in the order consistent with the order of packets' sizes in Figure 10 and the calculated values of  $\gamma_p$  are reasonable for bainitic matrix. The smaller packet size of the first group is corresponded to the higher  $\sigma_f$  and the higher impact energy.

#### C. Effects of High Degree Misorientation Boundaries

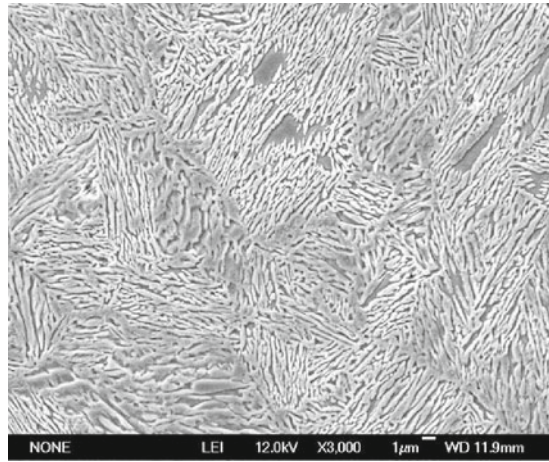
As stated in the introduction, Reference 7 revealed that bainitic packet size measured by EBSD with a

Table IV. Values of Charpy V Impact Toughness Measured at 223 K and 77 K (−50 °C and −196 °C) and Fracture Stress

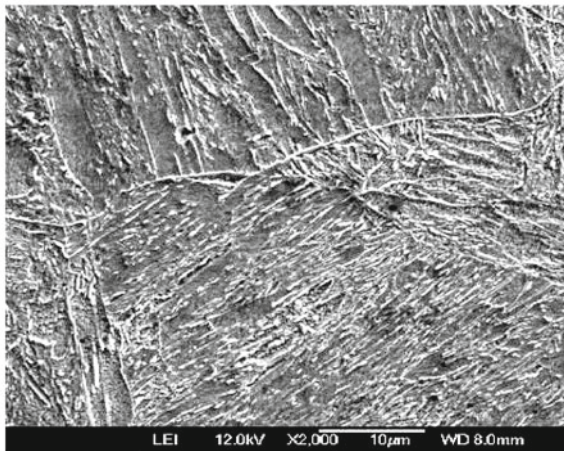
No.	$E$ (J) (223K [−50 °C])	$E$ (J) (77 K [−196 °C])	$a$ (μm)	$\sigma_f$ (MPa)	$\gamma_p$ (J/m <sup>2</sup> )	
First group	Base metal	177.3	44.2	22.0	2705	233.26
	T5-21	163.0				
Second group	DM4-1	24.5	5.9	39.7	1591	145.6
	M100	33.2	20.0	40.0	1988	136.6
	T100	61.2	3.9	37.7	1581	209.1

Note:  $E$ : impact toughness;  $a$ : area of fracture facet at the site of crack initiation;  $\sigma_f$ : fracture stress;  $\gamma_p$ : the effective surface energy.

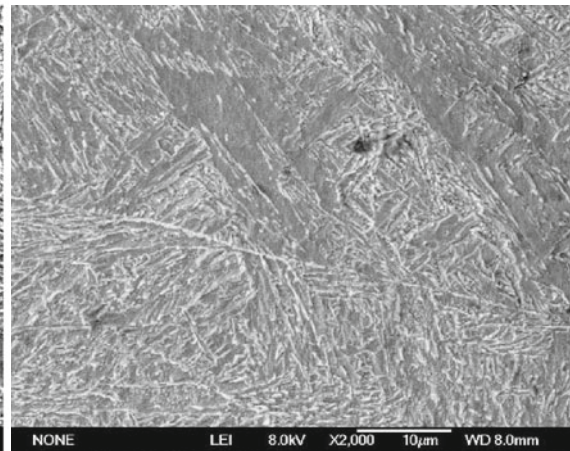




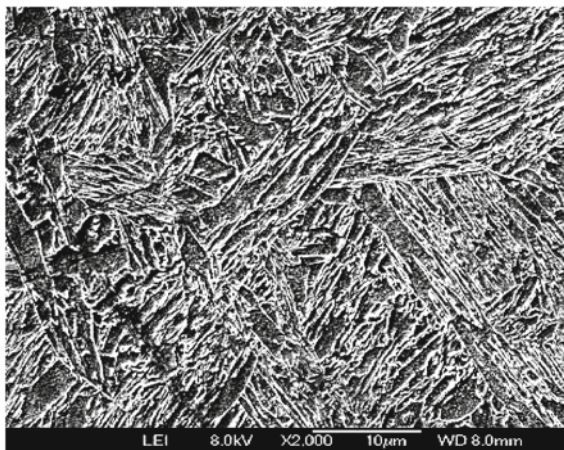
(a) Base metal



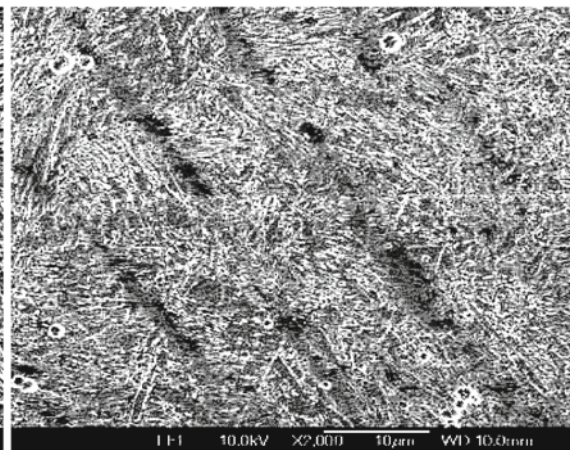
(b) T5-21



(c) DM4-1



(d) M100



(e) T100

Fig. 6—The microstructures of base metal and all weld metals (a), base metal (b), T5-21 (c), and M4- (d) M100 (e) T100.

15 deg misorientation criterion was about 3.5 times less than the value determined by optical microscopy, and it is identified as the microstructural unit controlling crack propagation in a cleavage fracture. Reference 11 showed that the effects of welding procedures, alloy content on

grain size distribution, and phase transformation in ferritic/martensitic welds were also analyzed by EBSD technology. References 12 and 13 systematically analyzed the orientation relationship between the lath martensite and the austenite by EBSD.



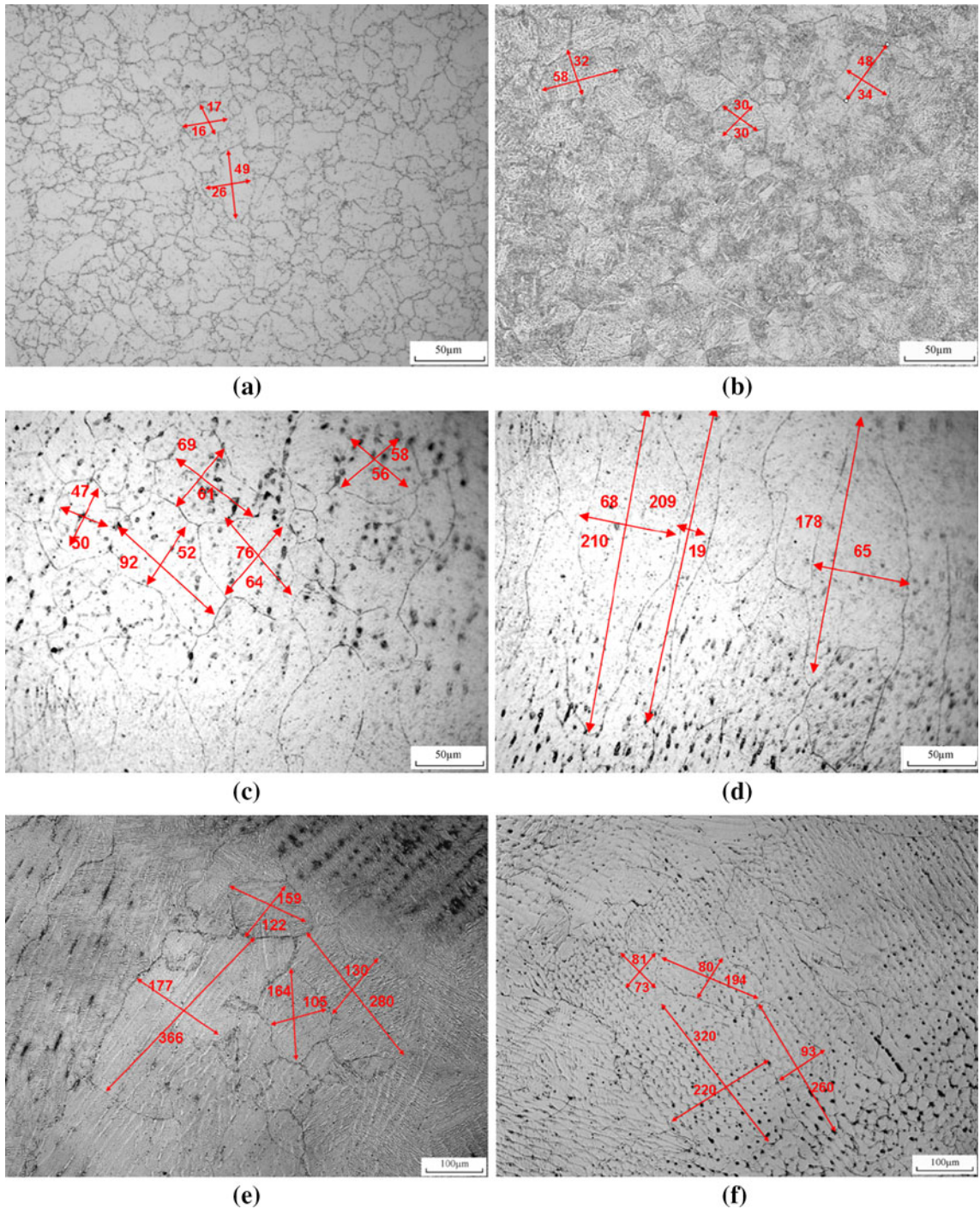


Fig. 7—Grain size measurement in (a) base metal, (b) T5-21, (c) DM4-1 center zone, (d) DM4-1 columnar zone, (e) M100, and (f) T100.

In this study, as seen in Figure 12, the sizes of the areas contained by the high-misorientation degree boundaries are appreciably smaller than the sizes of the bainitic packets; however, in Figure 14, the retained cracks are stopped by the packet boundaries rather than by the high misorientation degree boundaries in a packet. Thus, the cleavage fracture is controlled by the bainitic packet rather than by the area contained by the

high misorientation degree boundaries. In addition, as shown in Figures 11 and 12, appreciable differences of the densities of high degree misorientation boundaries revealed by EBSD between the first group of T5-21 and the second group of DM4-1 welds metal are not found. Surprisingly, the density of high degree misorientation boundaries in the base metal with high impact toughness is appreciably lower than that of the weld metals.

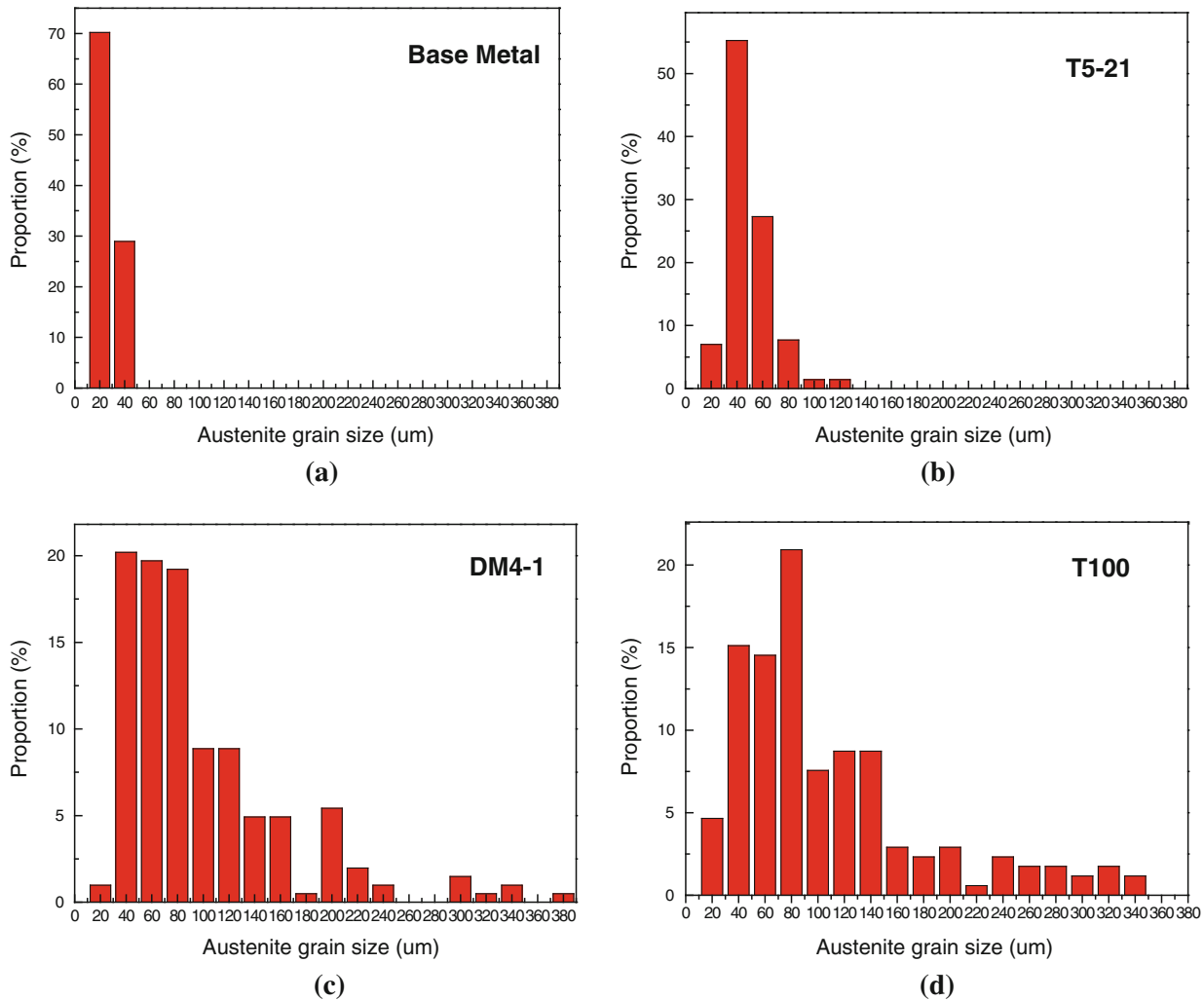


Fig. 8—The histograms of grain size measurements in (a) base metal, (b) T5-21, (c) DM4-1, and (d) T100.

Therefore, the superior impact toughness of the first group of base metal and T5-21 at 223 K ( $-50\text{ }^{\circ}\text{C}$ ) cannot be attributed to the density of high degree misorientation boundaries.

In Figure 16, by comparing the high misorientation degree boundaries and the fine tear ridges in the cleavage facets, it seems that the latter is produced by the former. Thus, in this study, the resistance to the cleavage cracking is mainly provided by the packet boundary, and the high misorientation degree boundaries offers some resistance and produces the fine tear ridges in the cleavage facets.

#### D. Decisive Microstructural Constituents

Based on the discussions carried out in Sections IV-A through IV-C, it is concluded that the decisive microstructural feature that determines the impact toughness in the notched bar is the bainite packet rather than the region contained by the high misorientation degree boundaries. The bainite boundary provides the main

resistance and makes the propagation of a packet-sized crack across the boundary the critical event for the cleavage fracture. The packet size specifies the critical cleavage facet and the local fracture stress  $\sigma_f$ . The reason why the values of impact toughness measured at 223 K ( $-50\text{ }^{\circ}\text{C}$ ) for the first group of the base metal and T5-21 are generally higher than those measured for the second group of the DM4-1, T100, and M100 is attributed to that the size of the bainitic packet of the first group is finer than that of the latter group. Figure 17 shows a typical comparison between the packet sizes of the DM4-1 weld metal and the T5-21 weld metal. It is apparently that the sizes of packets in T5-21 are appreciably smaller than that in DM4-1 weld metal. A general comparison of the grain or the packet sizes is summarized in Figure 10. The lengths of the critical events corresponding to the sizes of packets of the first group of the base metal and T5-21 are smaller than that of the second group of DM4-1, T100, and M100. This is the reason why the impact toughness of the metals of the first group is superior to that of the metals of the second group.

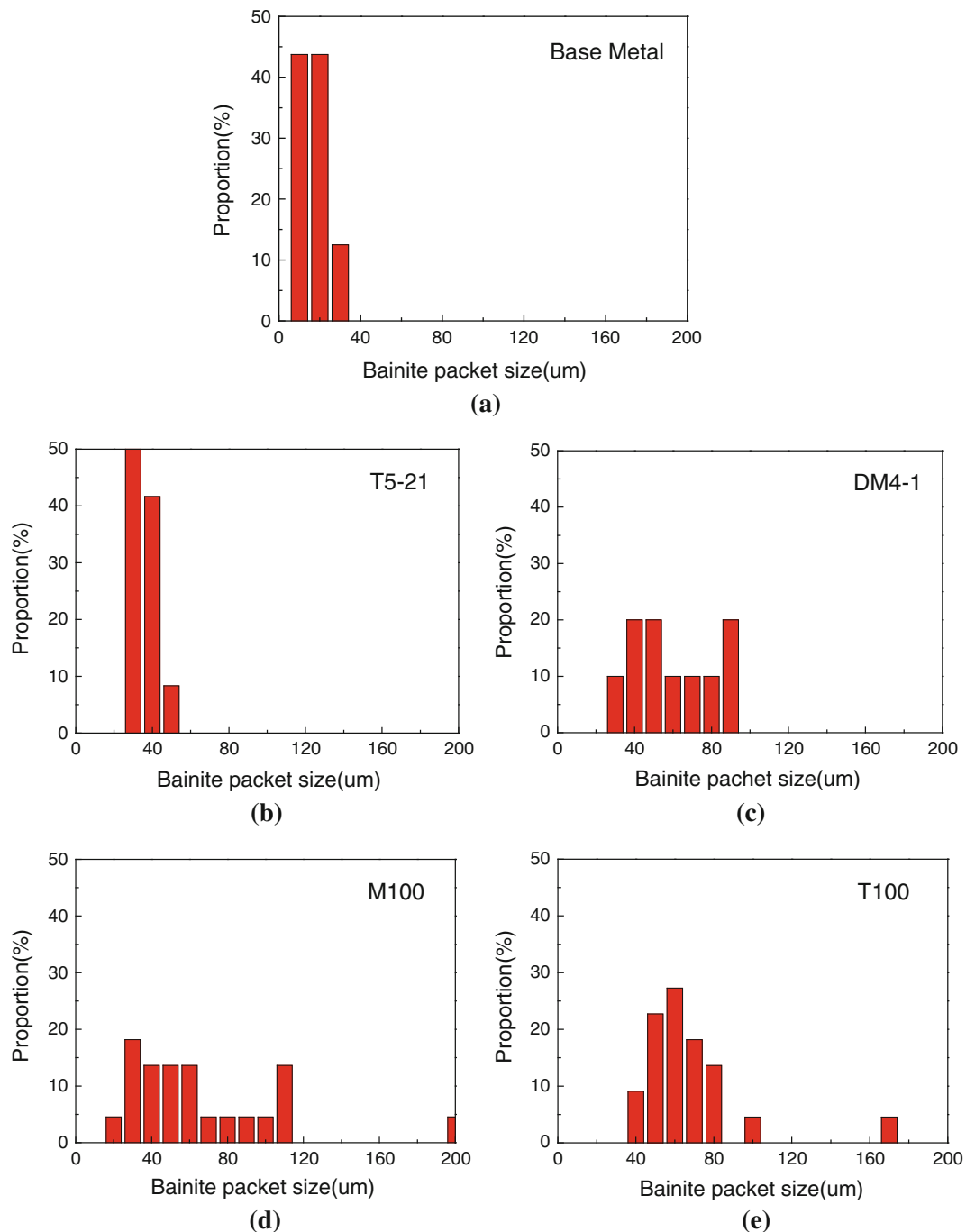


Fig. 9—The histograms of the packet sizes in microstructures of (a) base metal, (b) T5-21, (c) DM4-1, (d) M100, and (e) T100 weld metals.

### E. Effects of Nickel Addition

As indicated in the Introduction, Reference 8 revealed that regardless of packet size and yield strength, the addition of nickel gave rise to a decrease in Charpy V impact transition temperature of about 293 K (20 °C) per pct nickel. He attributed this effect to increasing the cleavage fracture resistance. In this work, at the first stage only the base metal BM, weld metal T5-21, and weld metal DM4-1 were used. The metals were divided into two groups: the first group

including the base metal BM and weld metal T5-21, which presents superior impact toughness (Table IV), and the second group including the weld metal DM4-1, which presents inferior toughness. From the composition point of view, the only appreciable distinction in alloy contents between these two groups was the differences in Ni contents: around 6 to 7 pct Ni for the first group and lower than 4 pct Ni for the second group. The effects of Ni addition were focused.



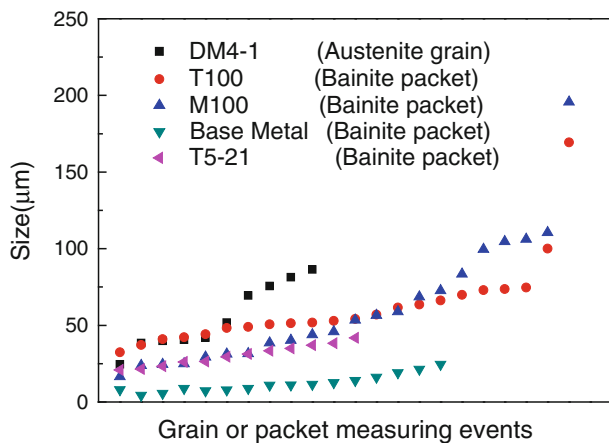


Fig. 10—The grain and packet sizes measured in successive events.

Table V compares the Ni-relative parameters between the two groups. As seen in Table V, the grain sizes of weld metals with higher Ni contents are finer. Besides the fine grain/packet sizes in the metals of the higher Ni content group, the fine bainitic laths and the higher fractions of the austenite-rich M-A constituent were observed. Because in steels with higher Ni content the flakes of the M-A constituent were found to be rich of austenite and have high plasticity,<sup>[1,14]</sup> both fine bainitic laths and Ni-rich M-A flakes cause denser higher misorientation boundaries and higher resistance by producing the fine tear ridges on the fracture surface. References 15 and 16 have shown that fine-film-retained austenite distributed between bainite laths contributes to higher toughness and ductility. The effect of Ni addition is considered to be decisive in the difference of impact toughness between these two groups. The mechanism of the improvement needs to be investigated in the future.

#### F. Effect of Welding Process

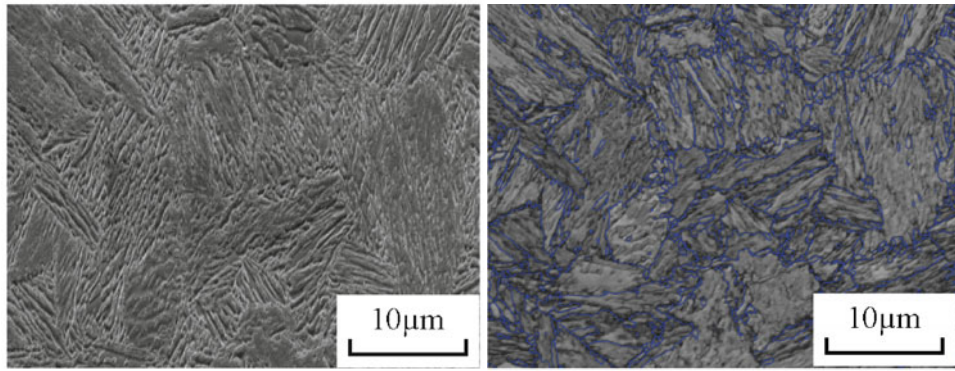
In Section IV-E, the positive effects of Ni content were discussed. However, as listed in Tables I, IV, and V, whereas the Ni content of 6.36 pct in T100 weld metal is comparable with that of 5.74 pct in T5-21, at 223 K (−50 °C), the impact toughness of 61.2J of the former is much less than that of 163J of the latter. For investigating the reason of the inferior toughness of M100 and T100, Table VI compares the values of Charpy V impact toughness and relevant parameters measured at 223 K (−50 °C) for weld metals of T5-21 and T100. From Table VI, the superior toughness of the T5-21 is attributed to its microstructural features: the fine grain sizes and the fine width of bainitic laths. From

Table VI, the area fraction of austenite-rich M-A flakes is higher for T5-21 than that for T100. The cause of the inferior microstructural features with lower toughness of T100 is attributed to the welding process. Figure 18 displays the macrostructure (Figures 18(a) through (d)) of T100 and DM4-1 and the fracture surface(s) of the weld metal T100. From Figure 18, it is evident that the coarse directional columnar grains exhibited in Figure 18(b) produce the coarse embossing fracture strips shown in Figure 18(e), which cause the inferior toughness of weld metal T100. Table VII lists the geometric and metallographic parameters measured in T100 and T5-21 weld metal, which shows that the width of the weld of T100 is appreciably larger than that of T5-21. It is considered to be welded by horizontal weaving of the welding torch. This procedure actually produces high heat even at the same welding current and causes larger columnar grains and segregation of impurities on the boundaries of the crystalline cells as shown in Figures 18(a) and (b). Therefore, regardless of the higher nickel content, the large columnar grains with impurity segregating boundaries make the impact toughness of the T100 weld metal inferior. The similar phenomenon was observed in the case of M100.

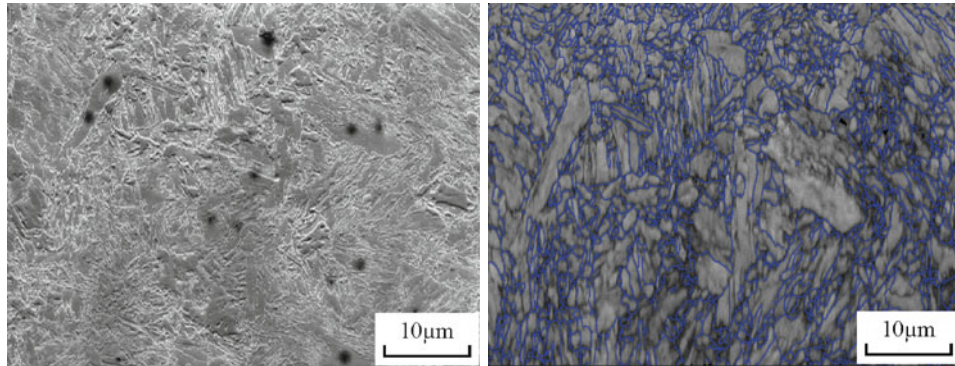
## V. CONCLUSIONS

The microstructural features that determine the impact toughness of the base metal and the weld metals of a 980 MPa 8 pct Ni high-strength steel were investigated in this work. The following conclusions are drawn:

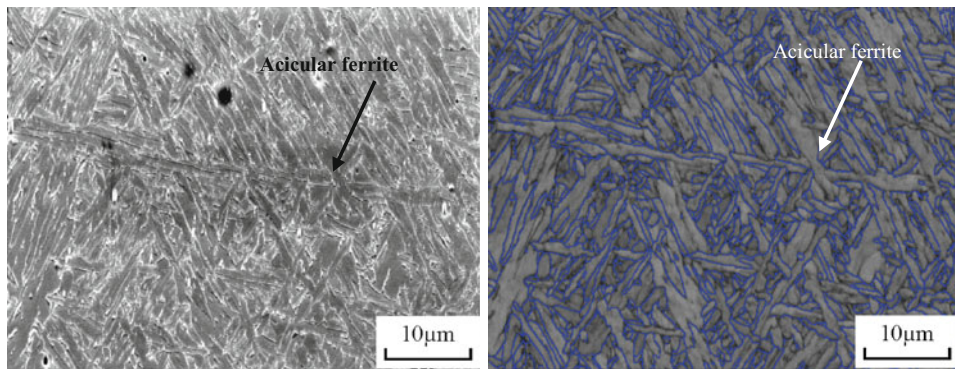
1. In the base metal and the weld metal of the 980 MPa 8 pct Ni high-strength steel, the critical event for cleavage fracture is the propagation of a bainite packet-sized crack across the packet boundary into contiguous packets. The bainitic packet sizes control the cleavage cracking and the impact toughness.
2. The high-angle misorientation boundaries detected in a bainite packet by EBSD form fine tear ridges on fracture surfaces and provide additional resistance to crack propagation. However, they are not the decisive factors controlling the cleavage fracture.
3. The effects of Ni content around 6 pct are essential factors for improving the toughness.
4. The extra large cleavage facets seriously deteriorate the toughness, which are formed on the interfaces of large column crystals growing in welding pools with high heat input.



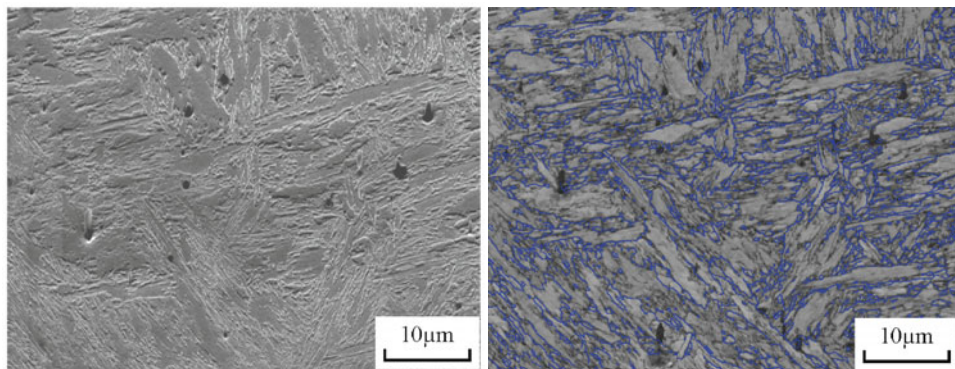
(a) Base metal



(b) T5-21

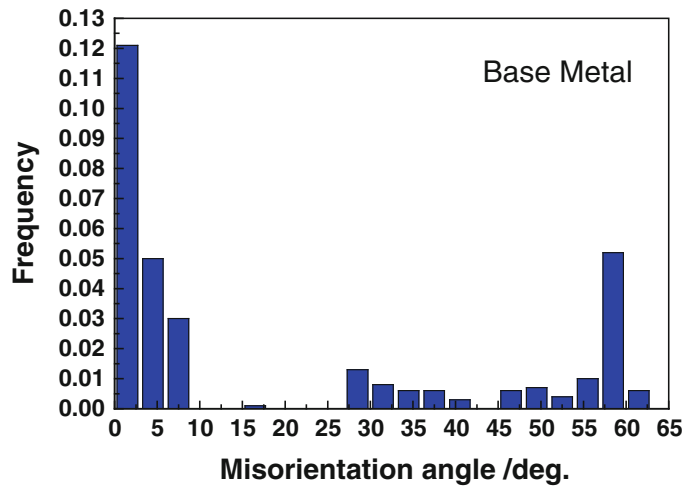


(c) DM4-1

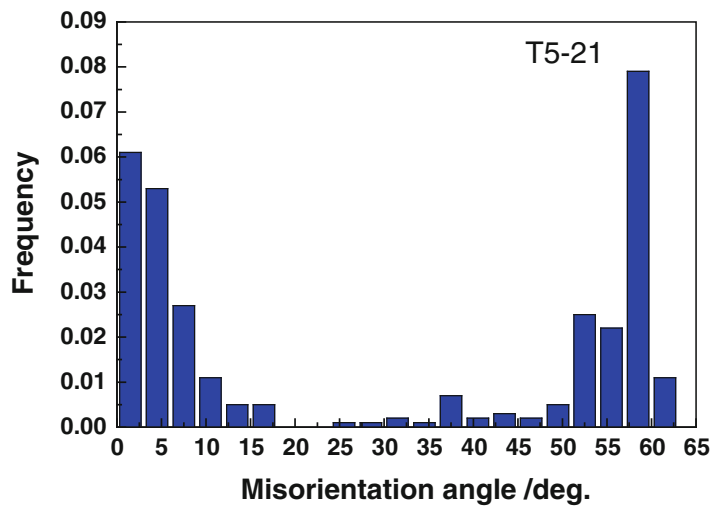


(d) M100

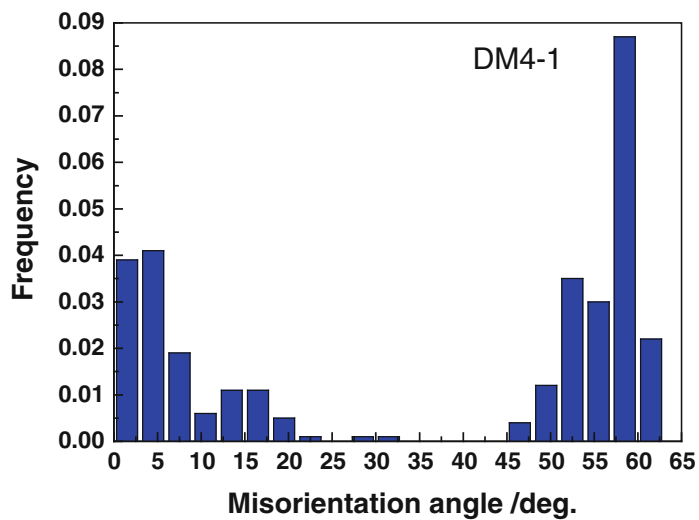
Fig. 11—The higher degree misorientation boundaries depicted by EBSD for (a) base metal and weld metals, (b) T5-21, (c) DM4-1, and (d) M100 weld metals.



(a)



(b)



(c)

Fig. 12—Histograms of the degrees of grain or packet boundaries of (a) base metal, (b) T5-21, and (c) DM4-1.



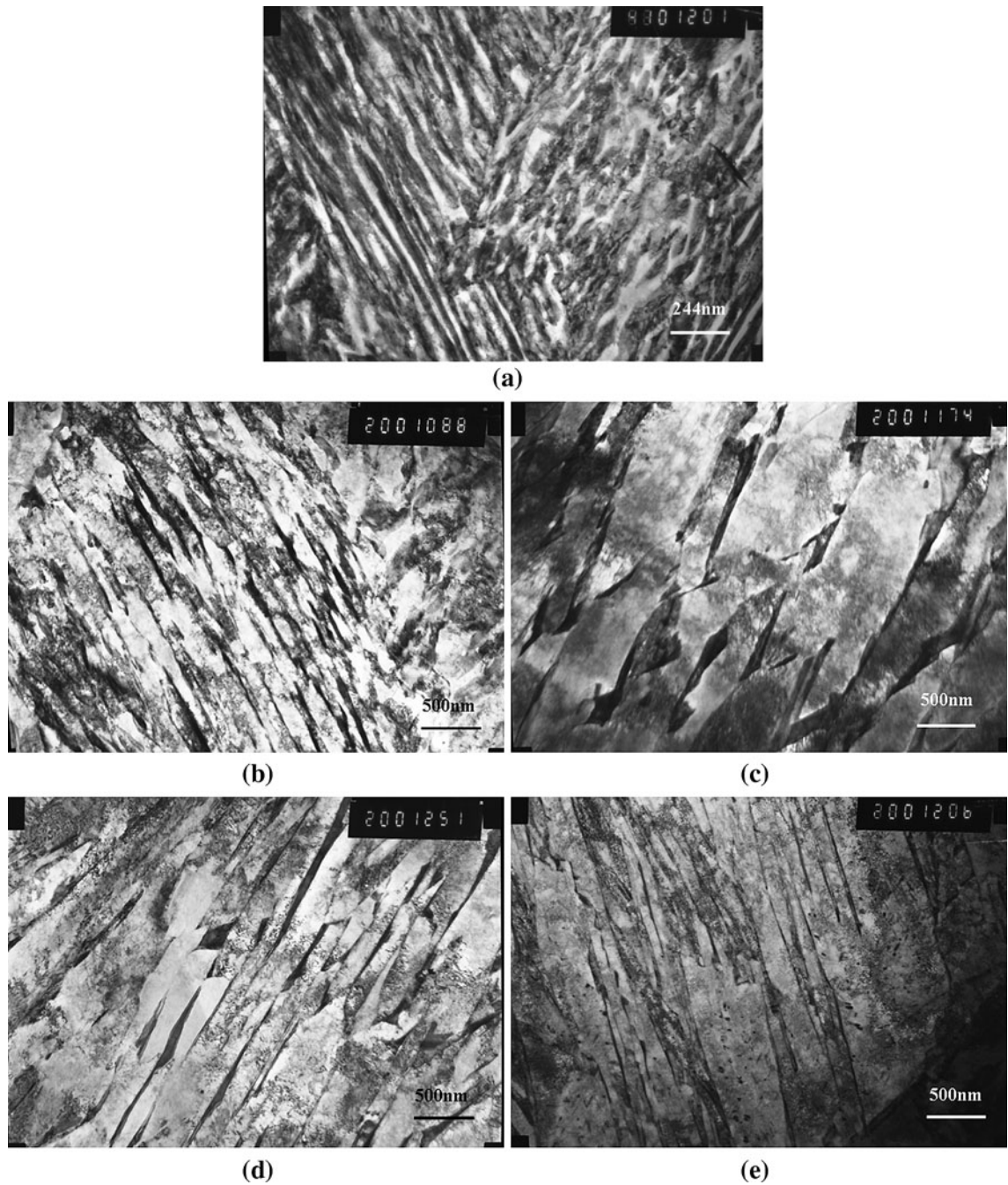
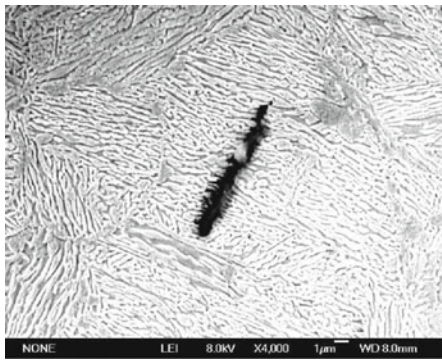


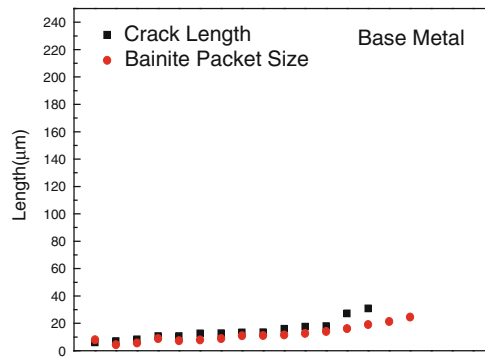
Fig. 13—TEM images of (a) base metal, (b) T5-21, (c) DM4-1, (d) M100, and (e) T100.

Table V. The Dimensions and Proportions of Phases

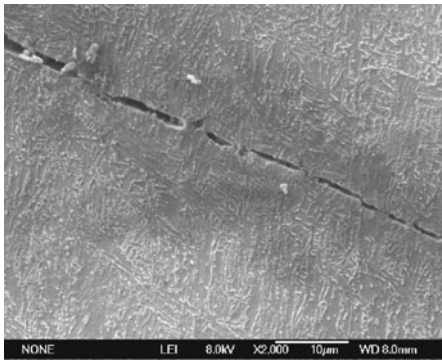
No.	Ni (pct)	Average Grain Size ( $\mu\text{m}$ )	$E_{[223 \text{ K } (-50 \text{ }^\circ\text{C})]}$ (J)	Width of Bainite Lath (nm)	Average Width of Bainite Lath (nm)	Area Fraction of Bainite (pct)	Area Fraction of austenite-Rich M-A (pct)
BM	7.58	20	177	20 to 80	34	42	58
T5-21	5.74	30	163	65 to 186	113	61	39
DM4-1	3.79	60	24.5	180 to 850	428	74	26



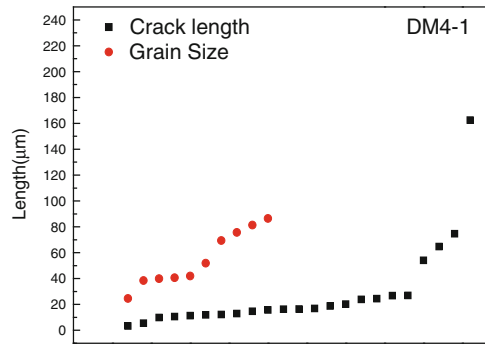
(a)



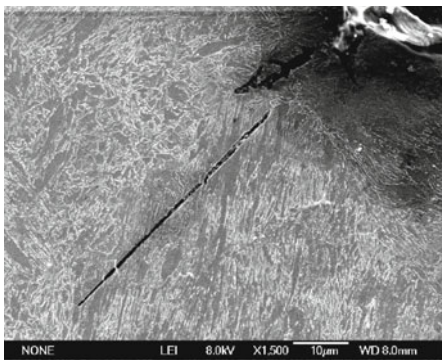
(b)



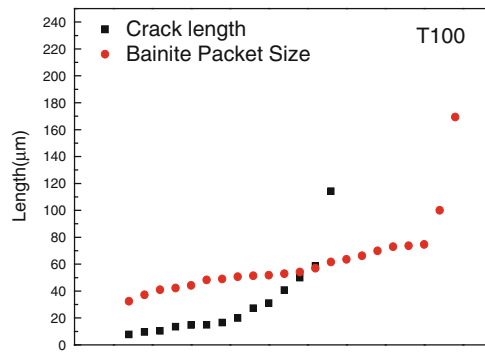
(c)



(d)



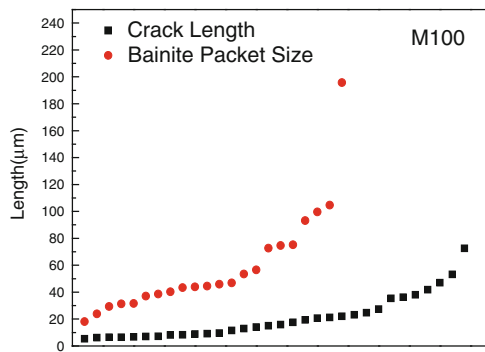
(e)



(f)



(g)



(h)

Fig. 14—The cracks retained in base metal and weld metal in Charpy V specimens fractured at 77 K (−196 °C) and the lengths of retained cracks and bainitic packets randomly measured by random event in (a, b) base metal, (c, d) DM4-1, (e, f) T100, (g, h) M100. The abscissa of (b, d, f, and h) is the measurement event.



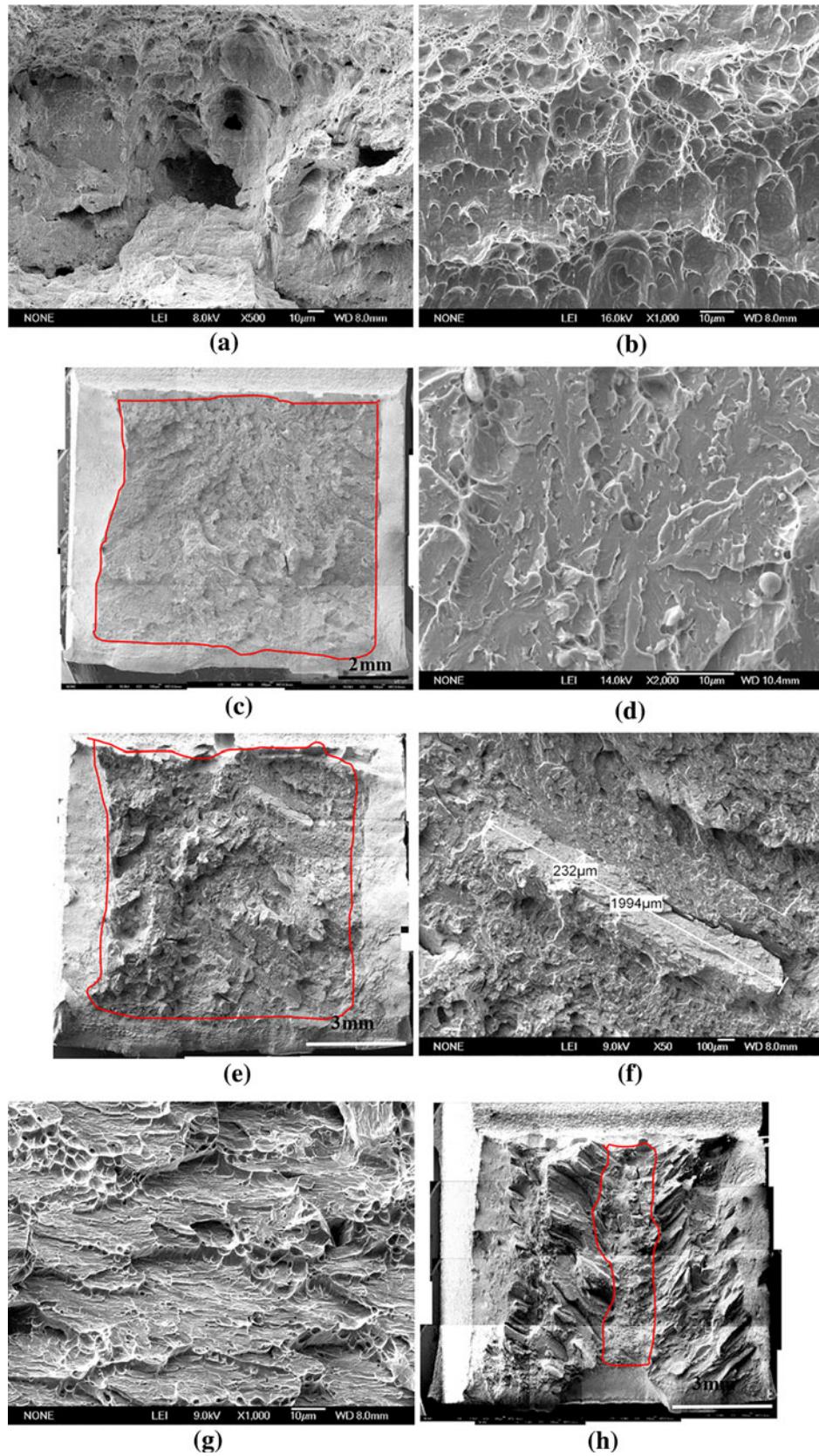


Fig. 15—Fracture surfaces of (a) base metal, (b) T5-21, (c, d) DM4-1, (e, f, and g) M100, (h, i, and j) T100 Charpy V specimens fractured at 223 K (−50 °C).



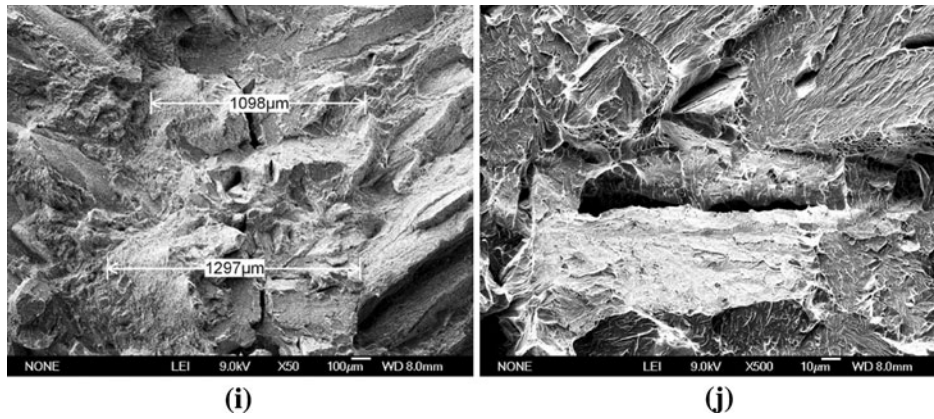


Fig. 15—continued.

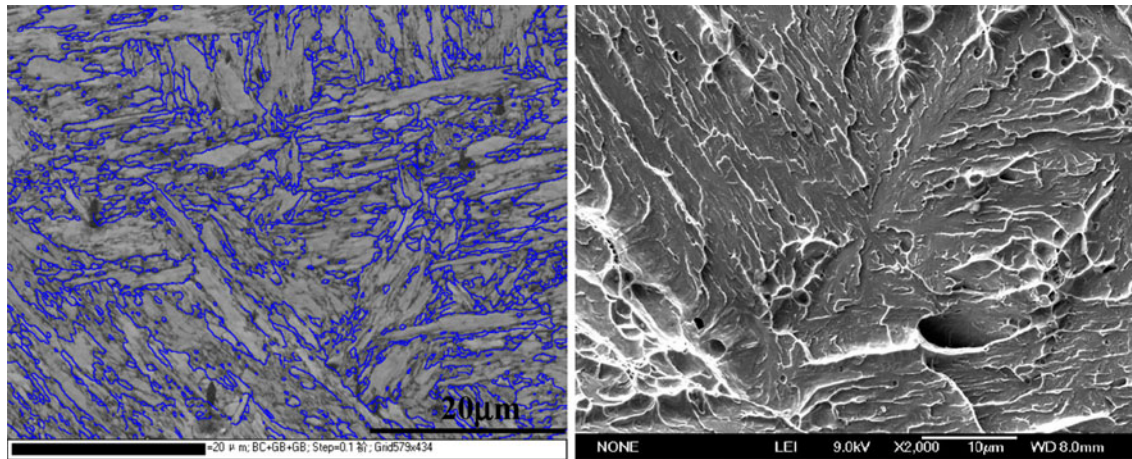


Fig. 16—Comparing the high misorientation degree boundaries and the fine tear ridges on the fracture surface.

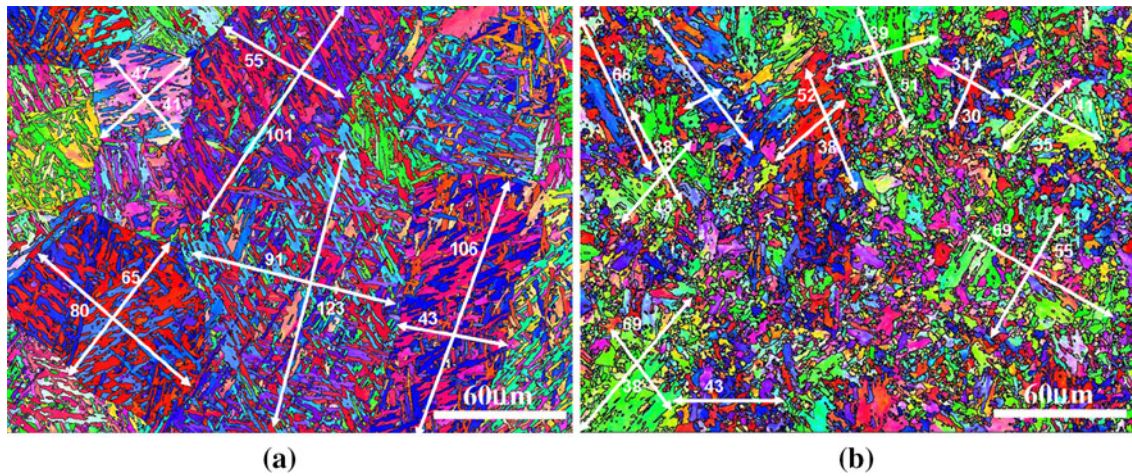


Fig. 17—Sizes of packets in (a) DM4-1 and (b) T5-21.

**Table VI. Parameters Relevant to Toughness in Weld Metal with Different Heat Input**

No.	$E_{(223 \text{ K } [-50 \text{ °C]})}$ (J)	Nickel (pct)	Average Grain Size ( $\mu\text{m}$ )	Width of Bainite Lath (nm)	Average Value (nm)	Area Fraction of M-A (pct)
T5-21	163	5.74	30	65 to 186	113	39
T100	61.2	6.36	60	59 to 578	151	26

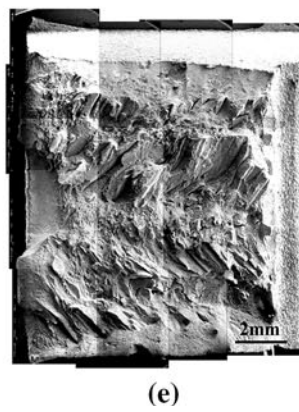
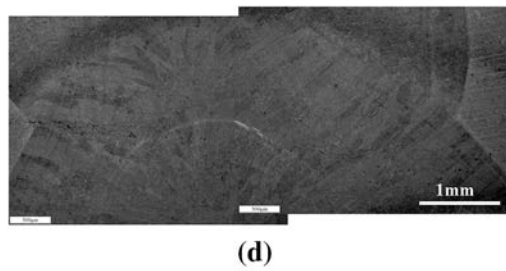
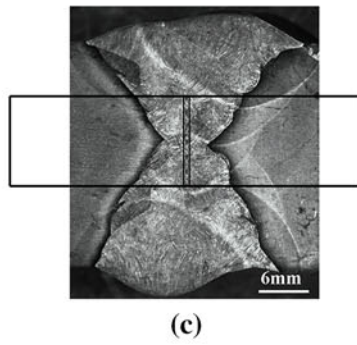
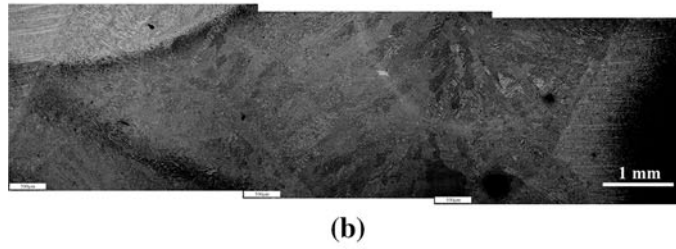
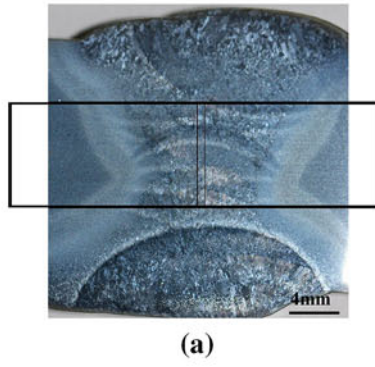


Fig. 18—The macrostructure of (a, b) T100, (c, d) DM4-1, and (e) the fracture surface of T100.

**Table VII. Metallographic Parameters Measured in T100 and T5-21 Weld Metal**

Weld Metal	Weld Width (mm)	Weld Depth (mm)	Columnar Grain Width (mm)	Sizes of Fine Grain (mm)
T5-21	15.9	7.4	0.29	0.11
T100	20	7.6	0.41	0.45
M100	14.3	8.5	0.47	0.16

### ACKNOWLEDGMENTS

This work was financially supported by the National Nature Science Foundation of China (Nos. 51035004 and 50905081).

### REFERENCES

1. R. Cao, W. Feng, Y. Peng, W.S. Du, Z.L. Tian, and J.H. Chen: *Mater. Sci. Eng. A*, 2010, vol. 528 A, pp. 631–42.
2. J.R. Low: *Deformation and Fracture in Solids*, Springer-Verlag, Berlin, Germany, 1956, pp. 163–76.
3. A. Kamada, N. Koshizuka, and T. Funakoshi: *Trans. ISIJ*, 1976, vol. 16, pp. 407–16.
4. G.T. Hahn: *Metall. Trans. A*, 1984, vol. 15, pp. 947–59.
5. W.J. Yang, B.S. Lee, Y.J. Oh, MY Huh, and J.H. Hong: *Mater. Sci. Eng. A*, 2004, vol. 379 A, pp. 17–26.
6. A. Echeverria and J.M. Rodrigues-Ibabe: *Mater. Sci. Eng. A*, 2003, vol. 346A, pp. 149–58.
7. L. Rancel, M. Gomez, S.F. Medina, and I. Gutierrez: *Mater. Sci. Eng. A*, 2011, vol. 530A, pp. 21–27.
8. L.A. Norstrom and O. Vingsbo: *Met. Sci.*, 1979, vol. 13, pp. 677–84.
9. R. Cao, Y.J. Yan, W.S. Du, Z.L. Tian, Y. Peng, and J.H. Chen: *Mater. Sci. Technol.*, 2011, vol. 27, pp. 145–55.
10. J.H. Chen, G.Z. Wang, C. Yan, H. Ma, and L. Zhu: *Int. J. Fract.*, 1997, vol. 83, pp. 105–20.
11. B.K. Narayanan, L. Kovarik, M.A. Quintana, and M.J. Mills: *Sci. Technol. Weld. Join.*, 2011, vol. 16, pp. 12–22.
12. S. Morito, X. Huang, T. Furuhashi, T. Maki, and N. Hansen: *Acta Mater.*, 2006, vol. 54, pp. 5323–31.
13. A.F. Gourgues-Lorenzon: *J. Electron Microsc.*, 2009, vol. 233, pp. 460–73.
14. J.H. Chen, Y. Kikuta, T. Araki, M. Yoneda, and Y. Matsuda: *Acta Mater.*, 1984, vol. 32, pp. 1779–88.
15. V. Miihkinen and D.V. Edmonds: *Mater. Sci. Technol.*, 1987, vol. 3, pp. 422–31.
16. V. Miihkinen and D.V. Edmonds: *Mater. Sci. Technol.*, 1987, vol. 3, pp. 432–40.